J. Fluid Mech. (2010), *vol.* 645, *pp.* 59–80.
doi:10.1017/S0022112009992540

A continuum approach to reproduce molecular-scale slip behaviour

H.-Y. HSU AND N. A. PATANKAR†

Department of Mechanical Engineering, Northwestern University, 2145 Sheridan Road, Evanston, IL 60208-3111, USA

(Received 19 January 2009; revised 29 September 2009; accepted 30 September 2009; first published online 2 February 2010)

In this work we explore if it is possible to reproduce molecular-scale slip behaviour by using continuum equations. To that end it is noted that molecular-scale slip is affected by three factors: (i) near the wall, the fluid experiences a potential because of the wall; (ii) the fluid density responds to that potential, and hence, fluid compressibility is relevant; and (iii) the fluid can lose momentum to the wall. To incorporate these features we simulate shear flow of a compressible fluid between two walls in the presence of a potential. Compressibility effect is found to be important only in the near-wall region. The slip length is calculated from the mean velocity profile. The slip-length-versus-shear-rate trend is similar to that in molecular dynamic calculations. First, there is a constant value of the slip length at low shear rates. Then, the slip length increases beyond a critical shear rate. Lastly, the slip length reaches another constant value if the wall momentum loss parameter is non-zero. The scaling for the critical shear rate emerges from our results. The value of the slip length increases if the wall potential is less corrugated and if the momentum loss to the wall is low. An understanding of the overall force balance during various slip modes emerges from the governing equations.

1. Introduction

No-slip boundary condition is typically used in continuum fluid dynamics. This implies that fluid adjacent to the surface of a solid boundary moves at the same tangential velocity as the solid. Liquid slip next to solid walls has received attention because of its relevance in micro- and nano-fluidic devices (see Urbakh *et al.* 2004; Majumder *et al.* 2005; Holt *et al.* 2006; Sholl & Johnson 2006). The resistance in micro- and nano-scale channels is large because of the viscous forces. In this case, slip next to the wall can be helpful to reduce the flow resistance and thus to reduce energy requirements.

Slip at the fluid–solid interface has been investigated experimentally, numerically and analytically (see Thompson & Troian 1997; Pit, Hervet & Leger 2000; Zhu & Granick 2001; Tretheway & Meinhart 2002; Choi, Westin & Breuer 2003; Bocquet & Barrat 2007; Martini *et al.* 2008*b* and the references therein). Molecular dynamic (MD) simulations have provided important insights into the mechanisms of slip. However, it remains unclear whether the molecular-scale slip behaviour can be reproduced using continuum equations.

† Email address for correspondence: n-patankar@northwestern.edu

There are several motivating factors to seek a continuum description of molecular-scale slip behaviour. (i) The first is to gain a fundamental understanding of the reasons why continuum equations have not reproduced molecular-scale slip behaviour and, consequently, to find out if this issue can be overcome by appending the continuum equations with terms corresponding to the physical mechanisms that cause the molecular-scale slip behaviour. (ii) There are many instances (Urbakh *et al.* 2004; Majumder *et al.* 2005; Holt *et al.* 2006; Sholl & Johnson 2006) where flow rates through nano-channels are claimed to be high compared with the flow rates predicted by classical results (e.g. Poiseuille law). Given that the classical-continuum-theory-based results are the reference point to quantify such flows, it is of interest to fundamentally understand, if possible, the molecular-scale slip behaviour in the context of continuum equations. (iii) MD simulations are expensive, and it would be useful to have a general way to incorporate the slip behaviour within Navier–Stokes equations. This can eliminate the need to carry out extremely expensive and cumbersome multi-scale computations in nano-scale problems.

There have been prior studies to model slip based on continuum equations that assume incompressible flow. For example, Priezjev, Darhuber & Troian (2005) compared the slip behaviour, on surfaces of patterned wettability, obtained from molecular dynamics and continuum simulations. Good agreement was found between MD and incompressible continuum calculations only when the length scale of the pattern was larger than the molecular length scale. Einzel, Panzer & Liu (1990), Miksis & Davis (1994), Wang (2003) and Priezjev & Troian (2006), among others, used continuum equations of an incompressible fluid to study the effect of surface roughness on slip. Priezjev & Troian (2006) found that continuum calculations were consistent with MD calculations only when the roughness scale was larger than the molecular length scales. Thus, a clear understanding of the kind of continuum model necessary to reproduce slip behaviour at molecular scales is still missing.

In the current work we focus on understanding what type of continuum model is necessary to reproduce the slip behaviour at molecular scales. The key objective is to reproduce the correct trends in the slip length versus the shear rate by using continuum equations such that the underlying mechanisms causing those trends are consistent with those identified in prior MD studies.

We show that to reproduce the molecular-scale slip behaviour using continuum equation it is essential to account for fluid compressibility. We use an *ad hoc* model of a compressible fluid with a body force because of a potential caused by the presence of the wall. An incompressible fluid model is not sufficient to reproduce the mechanisms that explain slip at molecular scales.

Once the viability of the approach is established, the limitations of the current *ad hoc* model are identified, and an extension of this work in the future to develop a quantitatively predictive model is discussed.

The current understanding of molecular-scale slip is summarized in § 2. Governing equations, model for the potential and non-dimensionalization will be presented in §§ 3–5. Results will be presented in § 6, outlook in § 7 and conclusions in § 8.

2. Background

For the purposes of the discussion in this paper, the slip velocity and slip length are defined in figure 1. It shows shear flow next to a wall, where the wall molecules (or atoms) are located at $y = 0$. This also implies that the wall is atomically smooth, and the effect of wall roughness is not considered in this work. The mean velocity of

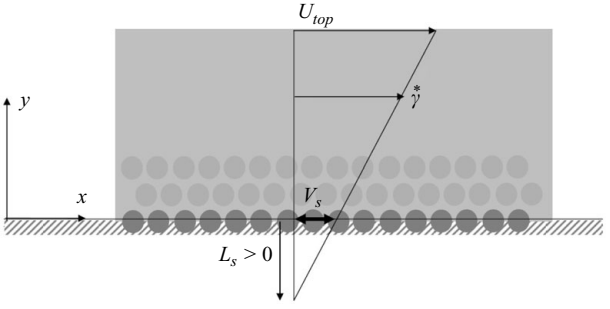

FIGURE 1. Definition of the slip velocity and slip length.

any wall molecule is zero. Next to the wall molecules are shown the first two layers of fluid molecules (or atoms). It will be discussed later that the first layer of fluid molecules plays a dominant role in the mechanism of slip. The location of the fluid molecules in the first layer corresponds to the first peak in the density profile of the fluid next to the wall.

The velocity profile of the fluid is linear away from the wall in a Couette flow. This profile when extrapolated to the location of the wall molecules, i.e. to $y = 0$, should give velocity equal to zero if the no-slip condition is valid. However, it is non-zero when there is slip. This is defined as the slip velocity V_s (see figure 1). The velocity profile of the fluid can also be extrapolated further to find the location at which the velocity is zero. That gives the slip length L_s (see figure 1). The slip velocity and slip length are related by

$$V_s = L_s \dot{\gamma}, \tag{2.1}$$

where $\dot{\gamma}$ is the shear rate as shown in figure 1.

Good insight into the mechanisms of slip is obtained from prior analytical and computational work in the literature (see Thompson & Troian 1997; Bocquet & Barrat 2007; Martini *et al.* 2008*b* and the references therein). Here we will specifically discuss the exposition by Lichter and co-workers (Lichter, Roxin & Mandre 2004; Martini *et al.* 2006, 2008*a*,*b*; Lichter *et al.* 2007) who have elucidated the various mechanisms of slip. The fluid molecules next to the wall experience an interaction potential (e.g. the Lennard–Jones potential). As a result, the fluid molecules tend to occupy locations of low potential along the wall and stay away from locations of high potential. Lichter and co-workers showed, by using MD and a new variable-density Frenkel–Kontorova model, that local defects in the occupancy of the low-potential locations propagate in the presence of shear. This leads to slip of the fluid molecules in the first layer at low shear rates. This was termed the defect propagation mechanism of slip (Lichter *et al.* 2004; Martini *et al.* 2008*b*). At high shear rates it was shown that slip occurs concurrently; i.e. the fluid molecules slip collectively rather than by defect propagation. In this case the wall potential does not play an important role; instead slip is primarily dependent on the dissipation of heat to the wall molecules (Lichter *et al.* 2004; Martini *et al.* 2008*b*). Thus, in this regime, slip depends on the high-shear-rate friction coefficient between the fluid and wall molecules.

The above results can be summarized by a plot of the slip length versus the shear rate (figure 2). At low shear rates the slip length is almost constant. After a critical shear rate the slip length increases. Martini *et al.* (2008*a*,*b*) showed that the rise in the slip length is unbounded if the wall molecules are fixed, i.e. if there is no dissipation of heat from the fluid molecules to the wall molecules. This is seen in the MD results

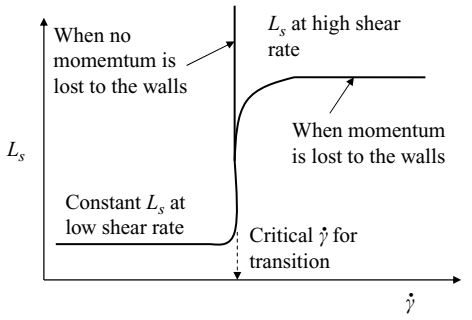

FIGURE 2. A schematic of the slip length versus shear rate behaviour from MD simulations.

by Thompson & Troian (1997). However, if the wall molecules have thermal motion, then heat can be dissipated to the wall molecules. Martini *et al.* (2008*a*,*b*) showed that in this case the slip length typically reaches another constant value at high shear rates after the transition.

In this work we ask the following question: is it possible to reproduce molecular-scale slip behaviour, described above, by using continuum equations? To that end we note that the continuum model must incorporate the following: (i) near the wall, the fluid experiences a potential because of the presence of the wall and correspondingly a force owing to the gradient in the potential; (ii) the fluid density responds to this potential, and hence, fluid compressibility is relevant; and (iii) the fluid loses momentum to the wall at high shear rates even if the wall potential does not play a significant role. To incorporate the above features, we simulate shear flow of a compressible fluid in the presence of a potential. A body force because of the potential is included in the momentum equation. Finally, a friction coefficient is used to capture the high-shear-rate dissipation at the wall.

It will be shown that this approach reproduces all the trends of the slip length discussed above.

3. Governing equations

Shear flow of a compressible fluid is considered in a configuration shown in figure 1. A two-dimensional domain is considered for simplicity. Steady-state conservation of mass for a compressible fluid is given by

$$\nabla \cdot (\rho \boldsymbol{u}) = 0, \tag{3.1}$$

where $\boldsymbol{u}$ is the velocity field and ρ is the density of the fluid. The steady-state momentum equation is

$$\rho(\boldsymbol{u} \cdot \nabla)\boldsymbol{u} = -\nabla p + \mu \nabla^2 \boldsymbol{u} + \frac{1}{3}\mu \nabla(\nabla \cdot \boldsymbol{u}) - \rho \nabla \phi, \tag{3.2}$$

where p is the thermodynamic pressure; μ is the fluid viscosity; and ϕ is the potential because of the presence of the wall. The last term, $-\rho\nabla\phi$, is the local body force per unit volume experienced by the fluid because of the potential. It will be seen that this term is crucial to reproduce the low-shear-rate slip behaviour. Gravity is not considered.

An equation of state is required for the compressible fluid. Here we make a simplifying assumption by considering an ideal-gas equation of state. The ideal-gas relation is strictly valid only at low pressures, where the fluid molecules do

not interact strongly with one another. For liquids at realistic pressures, additional correction terms are necessary to get quantitative accuracy. It will be seen from the results that this assumption is not restrictive to capture the qualitative aspects of slip that are of interest in this work. This is because it is the interaction between the fluid and the wall atoms that is crucial to qualitatively reproduce the slip behaviour. That is modelled through the potential term in the momentum equation. Extension to other fluids will be briefly discussed in § 7.

The ideal-gas state equation is

$$p = \rho R T, \tag{3.3}$$

where T is the temperature in Kelvin and R is the specific gas constant which depends on the molecular mass of the gas.

An isothermal system will be assumed. Hence, an energy equation for temperature will not be considered. This choice is based on two factors.

First, our work is motivated by computations based on prior MD simulations by others. In most of the prior MD investigations of interest in the current work, a constant temperature of the fluid phase is maintained by a thermostat for each liquid molecule (see Priezjev & Troian 2006; Martini *et al.* 2008*b* and the references therein). Our isothermal assumption is consistent with this – as it should be to enable appropriate comparison between the mechanisms of slip.

Second, it can be argued that the isothermal assumption is reasonable for the question of interest here. Viscous dissipation increases the temperature in the fluid mostly at high shear rates (Priezjev 2007*a*,*b*). Prior studies have shown that it is the fluid in the first layer that is critical to determining slip. Thus, the temperature rise in the first liquid layer is most relevant in terms of affecting slip. This temperature rise is suggested to be about 10 % (Priezjev 2007*a*,*b*) at high shear rates. The effect of the temperature on slip has been investigated in some prior studies (Guo, Zhao & Shi 2005*b*; Lichter *et al.* 2007; Priezjev 2007*b*). It is concluded that while the temperature rise changes the slip length, it does not change the fundamental mechanism of slip (see especially Lichter *et al.* 2007; Martini *et al.* 2008*b*). Since our focus in the present work is on fundamentally understanding what kind of continuum model is necessary to reproduce molecular-scale slip behaviour, we have chosen to consider an isothermal case similar to prior MD studies. A continuum model can indeed model the temperature effect by solving an additional energy equation, but that will not be the focus of the current work.

Our goal is to study slip next to a wall because of an imposed shear flow. To replicate that scenario, a non-zero potential ϕ is considered only next to the bottom wall. No potential is imposed next to the top wall. The potential ϕ will be discussed in § 4.

To impose a shear flow the x velocity component at the top boundary of the fluid domain is set to U_{top} (see figure 1). The y velocity component is zero. At the location of the bottom wall, i.e. at $y = 0$, the following Navier boundary condition is applied:

$$\mu \frac{\partial u}{\partial y} = \eta_w (u - U_b), \tag{3.4}$$

where u is the x component of fluid velocity; η_w is the friction coefficient at the wall; and U_b is the x velocity component of the bottom wall. In our simulations, we use $U_b = 0$; i.e. the bottom wall is stationary. The y velocity component of the fluid at $y = 0$ is set to zero. Periodic boundary conditions are used with respect to the x direction.

Some comments about the Navier boundary condition at $y = 0$ are in order. This condition by itself leads to slip between the fluid velocity and the wall velocity at $y = 0$. It will be seen that this boundary condition typically dominates the slip behaviour at high shear rates. Thus, η_w is a critical parameter to reproduce the high-shear-rate slip behaviour. It is the friction coefficient that would arise because of the heat dissipated to the wall molecules in MD simulations at high shear rates. If the wall molecules are assumed fixed, then no heat is dissipated to the wall (Martini *et al.* 2008*a*), and it would correspond to $\eta_w = 0$.

The governing equations are solved in a non-dimensional form (see § 5) using a commercial solver FLUENT (http://www.fluent.com/). Grid sensitivity tests were done to ensure that the solution is not dependent on the grid size.

4. The potential in the momentum equation

In this section, the choice of potential ϕ used in (3.2) is discussed. In prior results it has been suggested that the influence of the potential because of the wall on the first fluid layer is dominant (see for example Lichter *et al.* 2004). Thus, one approach to obtain ϕ is to suitably integrate the molecular potential imposed by the wall molecules on the fluid molecules. This would imply, for example, integrating the Lennard–Jones potential for the solid and fluid molecules. The potential computed by this approach will be called the 'wall potential' in this work.

Another approach is based on what will be called the 'effective potential' ϕ. The effective potential is deduced based on the density profile obtained from MD simulation of a stationary fluid next to the wall (see Bocquet & Barrat 2007; Raghunathan, Park & Aluru 2007 and the references therein). It is well known that this density profile shows undulations corresponding to the layering of fluid molecules next to the wall. Using this density profile, (3.2) with $\boldsymbol{u} = 0$ and the ideal-gas equation of state, ϕ is given by

$$\phi = -RT\ln\left(\frac{\rho_s}{\rho_{bulk}}\right), \tag{4.1}$$

where ρ_s is the density field from MD simulations of a stationary fluid and ρ_{bulk} is the density of the fluid far from the wall where the ϕ is zero.

The potential ϕ obtained from (4.1) is an effective potential experienced by the fluid. It is not equal to the wall potential; ϕ from (4.1) will be dominated by the wall potential in the first fluid layer. However, it will undulate beyond the first layer because of the undulations in the density profile obtained from stationary-state MD calculations. Thus, ϕ away from the wall is also influenced by the potential exerted by the fluid molecules on subsequent layers.

By using ϕ as obtained from (4.1) for shear flows as well, we assume that it is not strongly dependent on the shear rate. While this is a simplifying assumption, our results below show that it does not affect the qualitative nature of the slip behaviour.

In this work, for convenience of numerical simulation and parametric investigation, a potential function is used that emulates the potential obtained from (4.1) (Steele 1973),

$$\phi = \phi_{amp}\mathrm{e}^{-ky}\cos(my)(1.1 + b\sin(nx)), \tag{4.2}$$

where ϕ_{amp} is a parameter which controls the amplitude of the potential; k is a parameter for the exponential decay away from the wall; m and n are the wavenumbers for the undulations in potential along the x and y directions. The undulations in the

x direction are due to periodic spacing of the wall molecules along the wall, and the undulations in the y direction are due to the layering of fluid molecules. Adding 1.1 in the last part of (4.2) prevents ϕ from being equal to zero at $y = 0$, when $\sin(nx) = -1$. Furthermore, b is another parameter that determines the degree of corrugation of the potential ϕ. Larger b implies more corrugation and vice versa. To get this potential it is assumed that the centre of the wall molecules are located at $y = 0$; i.e. we do not consider the effects of surface roughness.

All computations in this work are done by using ϕ given by (4.2). The governing equations are solved in non-dimensional form. This is discussed in the next section.

5. Non-dimensionalization

The governing equations are solved in non-dimensional form. The following scales are used for non-dimensionalization:

$$\left.\begin{aligned}&[\text{length}] = h,\ [\text{density}] = \rho_{bulk},\ [\text{temperature}] = T_0,\\ &[\text{pressure}] = \rho_{bulk} RT_0,\ [\text{potential}] = RT_0,\ [\text{velocity}] = \sqrt{RT_0},\end{aligned}\right\} \tag{5.1}$$

where h is the height of the domain in the y direction (see figure 1) and T_0 is the constant specified temperature. The velocity scale $\sqrt{RT_0}$ is not the actual velocity scale of the flow, which is set by the velocity U_{top} of the top boundary of the domain. We keep U_{top} as a parameter of the problem, as is done in typical MD calculations.

Using the scales above, the momentum equation (3.2) can be rewritten in a non-dimensional form as follows:

$$\rho^*(\boldsymbol{u}^* \cdot \nabla^*)\boldsymbol{u}^* = -\nabla^* p^* + \mu^* \nabla^{*2}\boldsymbol{u}^* + \frac{1}{3}\mu^* \nabla^*(\nabla^* \cdot \boldsymbol{u}^*) - \rho^* \nabla^* \phi^*, \tag{5.2}$$

where the superscript $*$ denotes non-dimensional variables and μ^* is given by

$$\mu^* = \frac{\mu}{\rho_{bulk}\sqrt{RT_0}h}. \tag{5.3}$$

The non-dimensionalized continuity equation is given by

$$\nabla^* \cdot (\rho^* \boldsymbol{u}^*) = 0. \tag{5.4}$$

The dimensionless form of the ideal-gas equation of state becomes

$$p^* = \rho^*, \tag{5.5}$$

where $T^* = 1$ by the choice of the temperature scale and the fact that the temperature is assumed constant. Similarly, the non-dimensional form of the potential equation becomes

$$\phi^* = \phi_a \mathrm{e}^{-k^* y^*} \cos(m^* y^*)(1.1 + b^* \sin(n^* x^*)), \tag{5.6}$$

where $k^* = kh$, $m^* = mh$, $n^* = nh$, $b^* = b$ and $\phi_a = \phi_{amp}/RT_0$. This is the potential because of the bottom wall only. No potential is imposed next to the top wall.

The boundary condition at the top boundary is $u^* = U^*_{top}$, where $U^*_{top} = U_{top}/\sqrt{RT_0}$. At the bottom boundary, i.e. at $y^* = 0$, the Navier boundary condition in (3.4) becomes

$$\frac{\partial u^*}{\partial y^*} = f_w u^*, \tag{5.7}$$

where $f_w = (\eta_w h)/\mu$ is the non-dimensional wall friction coefficient.

6. Results

Equations (5.2) and (5.4)–(5.6) are solved together with the boundary conditions at the top and bottom boundaries. Periodic boundary conditions are used in the x^* direction. The non-dimensional channel height h^* and length L^* are equal to one.

In the non-dimensional equations presented above, the parameters of the problems are μ^*, U^*_{top}, f_w, ϕ_a, b^*, k^*, m^* and n^*. In the rest of this paper, dimensionless dependent variables will be denoted by the superscript $*$. Dependent variables without the superscript $*$ are dimensional.

Before presenting results in the following sections some remarks about the chosen parameters are necessary. Prior MD studies in the literature have been largely based on Lennard–Jones fluids. In those simulations (see Thompson & Troian 1997; Bocquet & Barrat 2007; Martini *et al.* 2008*b* and the references therein) the typical length scales are 1 nm; the time scales ($\tau \sim \sqrt{M\sigma^2/\epsilon}$, where M is the molecular mass, σ the scale of the molecular diameter and ϵ a Lennard–Jones parameter) are 10^{-12} s; and the sound speed ($\sim\sigma/\tau$) scales as $10^2\,\mathrm{m\,s^{-1}}$. The maximum imposed velocities typically range from 1 to $100\,\mathrm{m\,s^{-1}}$. Thus, the maximum shear rates are 10^9–$10^{12}\,\mathrm{s^{-1}}$. The typical Mach number is of the order of 10^{-2}. The Mach number reaches $O(1)$ in some cases if the shear rates are beyond the critical shear rates. The typical Reynolds numbers are 10^{-2}, whereas values $O(1)$ are obtained in some cases when the shear rates are above the critical shear rates.

Modern tribological systems, which have some of the largest shear rates, have lubricated films of the order of 1–2 nm, sliding velocities of the order of 1–$10\,\mathrm{m\,s^{-1}}$ and shear rates of the order of 10^9–$10^{10}\,\mathrm{s^{-1}}$ (see Bhushan 2000; Gao, Luedtke & Landman 2000). This implies a Mach number of the order of 10^{-2}–10^{-3} and a Reynolds number on the order of 10^{-2}.

The continuum-based calculations reported below are in terms of non-dimensional parameters which were chosen to be similar to the typical values in prior MD calculations. In our calculations, assuming air-like ideal gas, the speed of sound ($=\sqrt{RT_0}$ at isothermal conditions) scales as $300\,\mathrm{m\,s^{-1}}$ at ambient conditions with the length scale 1 nm and the time scale 10^{-12} s. The shear rates are typically 10^5–$10^{10}\,\mathrm{s^{-1}}$. Furthermore, U^*_{top} is a measure of the Mach number which is 10^{-7}–10^{-2} in most calculations. The Reynolds numbers are 10^{-8}–10^{-1}. The Reynolds number is at most $O(1)$, which happens in some cases in which the shear rates are beyond the critical shear rate.

6.1. *Effect of the shear rate on the slip length*

In this section the basic trends in the velocity profile and in the slip-length-versus-imposed-shear-rate plot are identified. The parameters chosen to solve shear flows are $\mu^* = 10$, $\phi_a = 0.01$, $k^* = 8.5$, $m^* = n^* = 16\pi$ and $b^* = 1$. First, we consider $f_w = (\eta_w h)/\mu \to \infty$ which implies that the fluid velocity $u = 0$ at $y = 0$ (i.e. at the location of the bottom wall).

The shear flow is solved for different value of U^*_{top} so that different shear rates are imposed above the bottom wall. The higher the value of U^*_{top}, the higher the imposed shear rate, and vice versa.

Figure 3 shows $\langle u\rangle/U_{top}$ with respect to y/h, where $\langle u\rangle$ is the value of the x component of fluid velocity that is averaged with respect to the x direction at any given y coordinate. It is seen that the normalized velocity profile has two limiting solutions. At high shear rates (i.e. large values of U^*_{top}) the normalized velocity profile is linear and does not change upon further increasing the imposed shear rate. At low

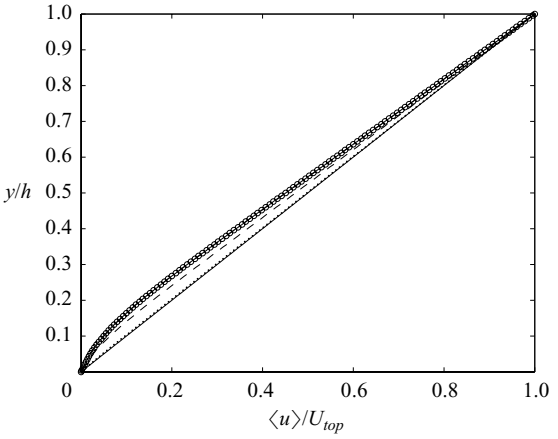

FIGURE 3. The mean velocity profile $\langle u\rangle/U_{top}$ versus y/h. The parameters are $\mu^* = 10$, $\phi_a = 0.01$, $k^* = 8.5$, $m^* = n^* = 16\pi$, $b^* = 1$ and $f_w \to \infty$: ——, $U^*_{top} = 1$; · · · · · ·, $U^*_{top} = 10^{-2}$; – – –, $U^*_{top} = 10^{-3}$; – · –, $U^*_{top} = 10^{-5}$; –o–, $U^*_{top} = 10^{-7}$.

shear rates (i.e. small values of U^*_{top}) the normalized velocity profile does not change upon further decreasing the imposed shear rate.

The imposed potential in (5.6) is sinusoidal with respect to the y direction to replicate the layering of fluid molecules next to the wall. Given our choice of $m^* = 16\pi$, this implies that the extent of the first layer is up to $y/h = 0.125$. It is seen from figure 3 that the low-shear-rate limiting velocity profile is nonlinear up to approximately $y/h = 0.125$ and linear beyond that. Thus, it is apparent that the first layer plays a dominant role by imposing an additional force that slows down the fluid next to the wall at low shear rates. This force balance and the mechanism of slip will be discussed further in § 6.2.

Prior studies based on MD simulations have reported linear velocity profiles in the channel. However, this is not necessarily at odds with the nonlinearity in the velocity profile in the first fluid layer in our continuum calculations. This is because the velocity profile from MD calculations is determined by averaging the velocities of the molecules in a bin whose width is typically of the order of one molecular diameter (i.e. about one fluid layer wide). Hence, any variation in velocity on the scale less than that is averaged and is not resolved. Indeed, the velocity profile from our continuum simulations, if presented based on bin averaging, is close to a linear profile even at low shear rates. This is consistent with the MD results.

The nonlinear velocity profile is also consistent with prior studies using kinetic-theory-based continuum approaches for liquids (Pozhar & Gubbins 1993; Din & Michaelides 1997). In those studies, the nonlinearity in the velocity profile was noted in the near-wall region and was reported in terms of an increase in the 'effective' viscosity of the fluid next to the wall. This is in agreement with the velocity profile in figure 3.

The transition from the limiting velocity profile in figure 3 at low shear rates to that at high shear rate occurs beyond a critical shear rate. During transition the velocity profile is intermediate between the two limiting profiles. The mean imposed shear rate $\langle\dot{\gamma}\rangle$ is calculated as the slope of the velocity profile beyond the first fluid layer. The non-dimensional slip length L_s/h is calculated by extrapolating the linear velocity profile obtained beyond the first fluid layer in figure 3 to the location of

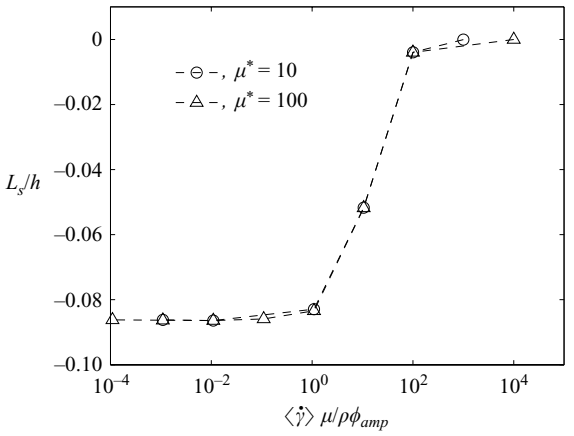

FIGURE 4. The plot of L_s/h versus non-dimensionalized shear rate for $\phi_a = 0.01$, $k^* = 8.5$, $m^* = n^* = 16\pi$, $b^* = 1$ and $f_w \to \infty$.

zero velocity (as depicted in figure 1). In the present case, the slip length is negative, since the intercept of the outer linear profile with the y/h axis happens above the coordinate of the wall (see the sign convention for the slip length in figure 1).

The slip length L_s/h calculated as discussed above is plotted in figure 4. It is seen that at low shear rates the slip length is constant. It transitions to another constant value at high shear rates. The constant slip lengths at low and high shear rates are a direct consequence of the limiting profiles of the normalized velocity at low and high shear rates, respectively, depicted in figure 3. This trend of the slip length is consistent with prior MD calculations (Martini *et al.* 2008*b*) and has been reproduced for the first time using a continuum approach. Similar to the correlation for the slip length developed by Thompson & Troian (1997), a correlation based on a logistic dose curve can be developed to fit the plot of the slip length versus the non-dimensional shear rate.

The estimation of the critical shear rate for transition will be discussed in § 6.2. It will also explain the scaling used for the imposed shear rate $\langle\dot{\gamma}\rangle$ in figure (4).

All calculations repeated with $\mu^* = 100$ resulted in no change in the slip length plot (see figure 4). Thus, μ^* does not change the slip length behaviour. This is expected because the inertia term is small in all the calculations. The flow Reynolds number $Re = (\rho_{bulk} U_{top} h)/\mu$ was at most of order one in the reported simulations.

The overall trend of the velocity profile remains the same irrespective of the friction parameter f_w in the Navier boundary condition at the bottom wall (3.4). Figure 5 shows velocity profiles for $f_w = 0.75$, and figure 6 shows profiles for $f_w = 0$. Reducing the friction coefficient compared with the cases in figure 3 leads to positive slip lengths at higher shear rate. The limiting velocity profile at high shear rate for $f_w = 0$ is vertical, which corresponds to an infinite slip length. The effect of f_w on the slip length will be discussed in further detail in § 6.3.

Next we will focus on explaining the low- and high-shear-rate behaviour discussed above and estimating the critical shear rate for transition.

6.2. *The mechanism of slip*

To understand the trends discussed in the previous section, we will focus on cases with the following parameters: $\mu^* = 10$, $\phi_a = 0.01$, $k^* = 8.5$, $m^* = n^* = 16\pi$, $b^* = 1$ and

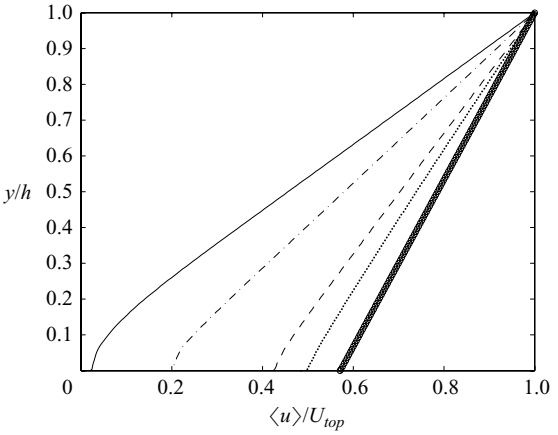

FIGURE 5. The mean velocity profile $\langle u\rangle/U_{top}$ versus y/h. The parameters are $\mu^* = 10$, $\phi_a = 0.01$, $k^* = 8.5$, $m^* = n^* = 16\pi$, $b^* = 1$ and $f_w = 0.75$: $-$o$-$, $U^*_{top} = 10^{+2}$; $\cdots\cdots$, $U^*_{top} = 3 \times 10^{-2}$; $- - -$, $U^*_{top} = 2 \times 10^{-2}$; $- \cdot -$, $U^*_{top} = 1.5 \times 10^{-2}$; ——, $U^*_{top} = 1 \times 10^{-5}$.

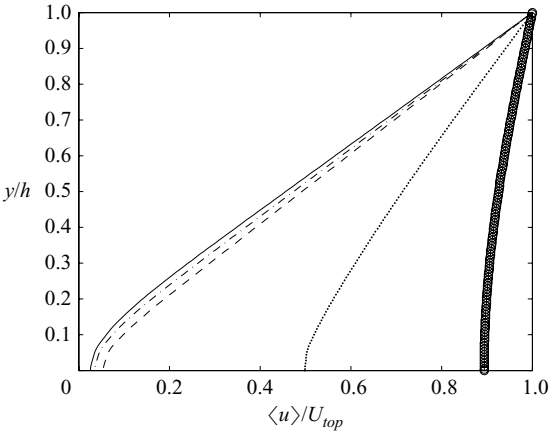

FIGURE 6. The mean velocity profile $\langle u\rangle/U_{top}$ versus y/h. The parameters are $\mu^* = 10$, $\phi_a = 0.01$, $k^* = 8.5$, $m^* = n^* = 16\pi$, $b^* = 1$ and $f_w = 0$: $-$o$-$, $U^*_{top} = 10^{-2}$; $\cdots\cdots$, $U^*_{top} = 2 \times 10^{-3}$; $- - -$, $U^*_{top} = 10^{-3}$; $- \cdot -$, $U^*_{top} = 5 \times 10^{-4}$; ——, $U^*_{top} = 1 \times 10^{-6}$.

$f_w = 0.75$. The normalized velocity profiles corresponding to this case are shown in figure 5 at different values of the imposed shear rate.

As discussed earlier, the velocity profiles at low shear rates imply that there is a net body force in the x direction acting in the first layer of fluid molecules next to the wall. At high shear rates this body force is unimportant as indicated by the linear velocity profile in the high-shear-rate limit. To understand the origin of this body force we consider the momentum equation (3.2). Given that inertia is unimportant (even if inertia were important this contribution would be zero because of the periodic boundary condition in the x direction, which is similar to a fully developed flow assumption), that the flow is in steady state and that there is no net pressure gradient imposed in the x direction, the only source for the net body force in the x direction

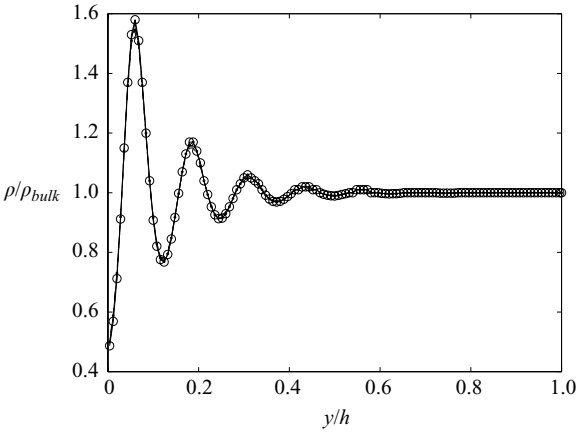

FIGURE 7. The density profile with respect to y/h at $x/h = 0.5$. The parameters are $\mu^* = 10$, $\phi_a = 0.01$, $k^* = 8.5$, $m^* = n^* = 16\pi$, $b^* = 1$ and $f_w = 0.75$: —o—, $U^*_{top} = 10^2$; · · · · · ·, $U^*_{top} = 2\times10^{-2}$; — — —, $U^*_{top} = 1.5 \times 10^{-2}$; — · —, $U^*_{top} = 10^{-2}$; ——, $U^*_{top} = 10^{-5}$. Note that the curves are nearly coincident and therefore indistinguishable from the curve for $U^*_{top} = 10^2$.

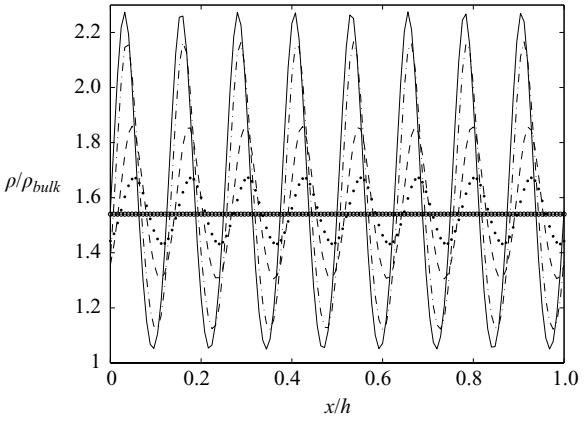

FIGURE 8. The density profile with respect to x/h at $y/h = 0.06$. The parameters are $\mu^* = 10$, $\phi_a = 0.01$, $k^* = 8.5$, $m^* = n^* = 16\pi$, $b^* = 1$ and $f_w = 0.75$: —o—, $U^*_{top} = 10^2$; · · · · · ·, $U^*_{top} = 2\times10^{-2}$; — — —, $U^*_{top} = 1.5 \times 10^{-2}$; — · —, $U^*_{top} = 10^{-2}$; ——, $U^*_{top} = 10^{-5}$.

is the term because of the potential ϕ, i.e. $-\rho\nabla\phi$. The force because of the potential is dependent on the density profile. Hence, we consider that next.

6.2.1. *Density profiles at high and low shear rates*

Figure 7 shows the density profile with respect to the y direction at $x/h = 0.5$ which is the mid-axial location of the computational domain (similar plots can be drawn for other x locations). It is seen that the density profile shows layering, as expected, because of the imposed potential ϕ. This profile does not change significantly with the imposed shear rate. Specifically, the locations of peaks and valleys remain unchanged.

Figure 8 shows the density profile with respect to the x direction at $y/h = 0.06$ which is the location of the first peak in fluid density next to the wall (see figure 7). It is seen that the density profile strongly depends on the imposed shear rate. As the shear rate increases there are two effects: the peaks are reduced, and they shift.

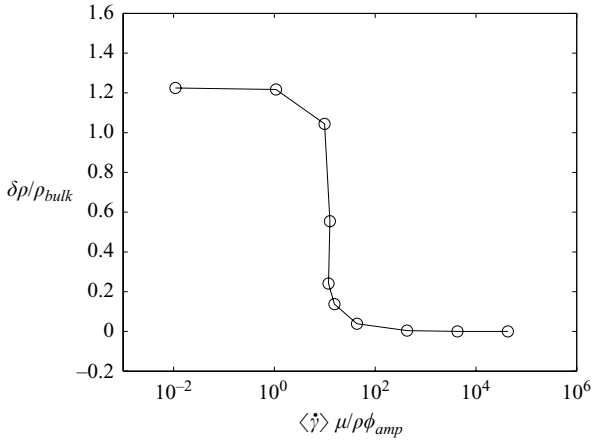

FIGURE 9. Plot of $\delta\rho/\rho_{bulk}$ versus $\langle\dot{\gamma}\rangle\mu/\rho\phi_{amp}$ that includes cases depicted in figure 8.

At high shear rates the density profile is almost constant with no undulations. The reduction of undulations in the density profile with respect to the imposed shear rate is quantified in figure 9, where $\delta\rho = \rho_{max} - \rho_{min}$; $\delta\rho$ is calculated based on the density profiles as shown in figure 8. Figure 9 delineates two distinct zones – one at low shear rates and another at high shear rates with a transition region beyond a critical shear rate. These low- and high-shear rate-regions are in one-to-one correspondence with the limiting velocity profiles at low and high shear rates, respectively, shown in figure (5).

The above trend in the density profile with respect to the x direction is consistent with the results based on molecular methods by Lichter *et al.* (2004, 2007) and Martini *et al.* (2006, 2008*a*,*b*). Specifically, the low-shear-rate density profiles are consistent with the molecular-scale mechanism of slip in the defect propagation regime. In this regime the time that the molecules spend in low-potential wells near the solid wall changes. Because of the imposed shear stress on the liquid molecules in the first layer, the equilibrium location of the molecules shifts leading to an axial shift in the density profile (see Lichter *et al.* 2004, 2007). This results in a density profile that is identical to that in our simulations. In our simulations also the shift in density profile is due to balance between the shear force and the force because of the wall potential. Our steady-state result gives a density profile that would be obtained by averaging the MD calculations over a long-time scale.

The near-constant-density profile with respect to the x direction at high shear rates is also consistent with the molecular-scale mechanism of collective slip (see Lichter *et al.* 2004; Martini *et al.* 2008*b*). Thus, our approach is a valid continuum representation of the molecular-scale dynamics that are relevant to reproduce the appropriate slip behaviour.

6.2.2. *Force balance at low and high shear rates*

The force balance is considered next to explain the nonlinear velocity profile at low shear rates and the linear velocity profile at high shear rates (figure 5). Integrating the x component of (3.2) with respect to the x direction leads to the following equation:

$$\mu\frac{\mathrm{d}^2\langle u\rangle}{\mathrm{d}y^2} = \left\langle \rho\frac{\partial\phi}{\partial x}\right\rangle, \tag{6.1}$$

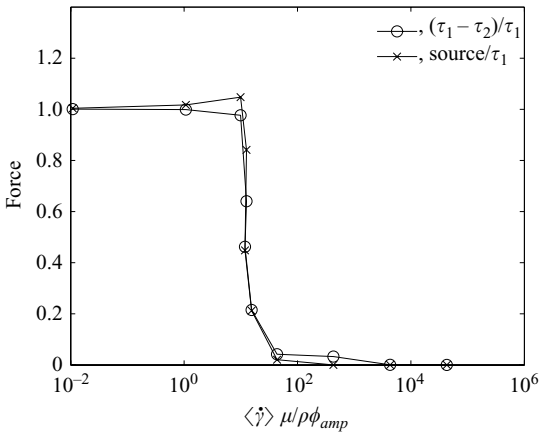

FIGURE 10. Verification of force balance given by (6.2). The variable 'source' is the net body force because of the potential given by the right-hand side of (6.2). The parameters are the same as those for figures 5 and 8.

where $\langle\cdot\rangle$ indicates average with respect to the x direction. Integrating this equation with respect to the y direction yields

$$\tau_1 - \tau_2 = \int_0^h \int_0^L \rho \frac{\partial \phi}{\partial x} \, \mathrm{d}x \, \mathrm{d}y, \tag{6.2}$$

where τ_1 is the total shear force on the fluid at the top boundary of the domain and directed in the positive x direction and τ_2 is the total shear force on the fluid at the bottom boundary of the domain and directed in the negative x direction.

The limiting velocity profiles, at low and high shear rates in figure 5, can be discussed in the context of (6.1) and (6.2). At low shear rates, the body force because of the potential on the right-hand side of (6.1) is non-zero in the first layer of fluid molecules and rapidly decays in the outer regions. That gives rise to a velocity profile for $\langle u \rangle$ that is nonlinear in the first layer and linear beyond that. Consequently, the total shear forces at the top and bottom walls are different with the difference being equal to the right-hand side of (6.2).

At high shear rates, the density profile is almost constant with respect to the x direction (figures 8 and 9). The body force because of the potential on the right-hand sides of (6.1) and (6.2) is zero if the density does not vary with the x direction. Thus, the force because of the wall potential plays no role in the force balance at high shear rates. It follows from (6.1) that $\tau_1 - \tau_2 = 0$, and the velocity profile for $\langle u \rangle$ is linear. This is in agreement with the velocity profiles in figure 5.

All the terms in (6.2) can be calculated from the numerical solution. In figure 10 we confirm that (6.2) is indeed satisfied by the numerical results. The plots for the left- and right-hand sides of (6.2) are in excellent agreement at all values of the imposed shear rates. Specifically, it is noted that the body force because of the potential is important only at low shear rates and is negligible at high shear rates. This is consistent with the trends of the velocity and density profiles discussed above.

It was confirmed that the above force balance is valid for all the cases considered in this paper.

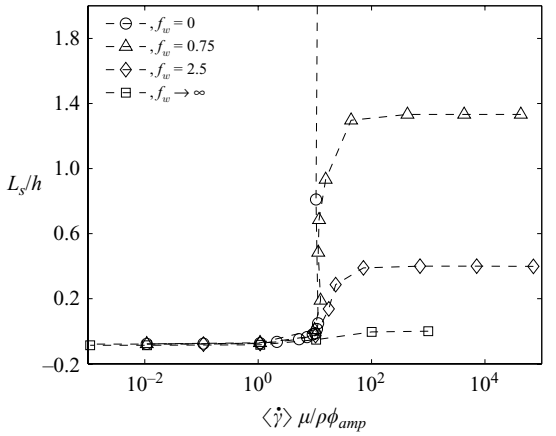

FIGURE 11. The slip length as a function of the non-dimensional shear rate at different values of $f_w = \eta_w h/\mu$. The fixed parameters are $\mu^* = 10$, $\phi_a = 0.01$, $k^* = 8.5$, $m^* = n^* = 16\pi$ and $b^* = 1$.

6.2.3. *Estimation of the critical shear rate for transition*

The scale of the body force term because of the potential, on the right-hand side of (6.1), is $\rho_{bulk}\phi_{amp}b/\lambda$, where λ is the wavelength of the potential ϕ along the x direction. Similarly, the scale of the net viscous force on the left-hand side of (6.1) is $\mu U_{top}/h\lambda$ in the first fluid layer. At high shear rates the viscous term dominates the body force because of the potential. Thus, for transition from low-shear-rate behaviour to high-shear-rate behaviour to occur the following condition must be satisfied:

$$\frac{\langle\dot{\gamma}\rangle\mu}{\rho_{bulk}\phi_{amp}b} \gg 1, \tag{6.3}$$

where it is assumed that $\langle\dot{\gamma}\rangle \sim U_{top}/h$ and $\mathrm{e}^{-k^*y^*} \sim O(1)$ near the wall. This is in agreement with the results shown in figures 4, 9 and 10. It is also in qualitative agreement with the estimate based on molecular-scale analysis by Martini *et al.* (2008*b*).

Equation (6.3) also explains the non-dimensionalization of the shear rate $\langle\dot{\gamma}\rangle$ used in presenting the results for the slip length as a function of the shear rate.

6.3. *Effect of friction coefficient f_w on the slip length*

At high shear rates, the limiting velocity profile is linear and is determined completely by the boundary condition at the top and bottom boundaries. Thus, the slip length at high shear rate is fully determined by the friction coefficient f_w. This will be shown in this section.

To study the effect of the friction coefficient, especially at high shear rates, simulations with the following parameters are considered: $\mu^* = 10$, $\phi_a = 0.01$, $k^* = 8.5$, $m^* = n^* = 16\pi$ and $b^* = 1$. Different values of f_w are chosen. For each value of f_w, shear flows are solved for a range of values of U^*_{top}. As discussed in § 6.1, velocity profiles for different imposed values of shear rate are plotted, and the slip length is computed.

Figure 11 shows a plot of the slip length versus the non-dimensional shear rate for different values of f_w. It is seen that the slip length is constant at low shear rates and increases beyond the critical shear rate as estimated in (6.3). The slip length at high shear rates is unbounded if $f_w = 0$ and is equal to another constant value for non-zero

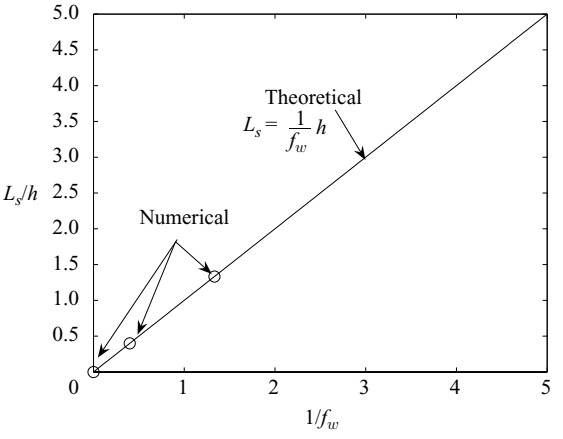

FIGURE 12. A comparison of the slip length obtained from figure 11 with the theoretical prediction in (6.7).

values of f_w. Thus, the high-shear-rate slip length crucially depends on f_w. It arises because of heat dissipated to the solid molecules as shown in prior MD simulations by Martini *et al.* (2008*a*,*b*). They also noted that if MD calculations are done with rigidly fixed wall molecules, then the liquid molecules cannot dissipate heat to the wall molecules. This would imply that the effective friction coefficient $f_w = 0$ for such simulations. These type of simulations were reported by Thompson & Troian (1997). Their slip length was indeed unbounded in agreement with the trend in figure 11.

Next we quantitatively verify that the high-shear-rate slip length in our computations is solely determined by f_w. At high shear rates the x-averaged velocity $\langle u \rangle$ is governed by

$$\frac{\mathrm{d}^2\langle u \rangle}{\mathrm{d}y^2} = 0, \tag{6.4}$$

which follows from (6.1) and the fact that the body force because of the potential is negligible. The x-averaged boundary conditions become

$$\left.\begin{aligned} &\langle u \rangle = U_{top}, \ \text{at } y = h, \\ &\mu \frac{\mathrm{d}\langle u \rangle}{\mathrm{d}y} = \eta_w \langle u \rangle, \ \text{at } y = 0. \end{aligned}\right\} \tag{6.5}$$

The solution for $\langle u \rangle$ is

$$\frac{\langle u \rangle}{U_{top}} = \frac{1}{(f_w + 1)} \left(f_w \left(\frac{y}{h} \right) + 1 \right). \tag{6.6}$$

We verified that the high-shear-rate limiting velocity profiles are the same as that given by (6.6) for all the cases considered. The slip length at high shear rate follows from the Navier boundary condition:

$$\frac{L_s}{h} = \frac{\mu}{\eta_w h} = \frac{1}{f_w}. \tag{6.7}$$

Figure 12 shows that the slip length obtained from figure 11 is in agreement with the theoretical prediction in (6.7).

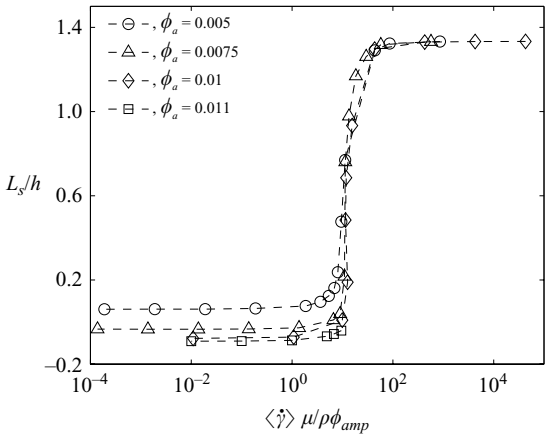

FIGURE 13. The slip length as a function of the non-dimensional shear rate for different values of ϕ_a. The fixed parameters are $\mu^* = 10$, $k^* = 8.5$, $m^* = n^* = 16\pi$, $b^* = 1$ and $f_w = 0.75$.

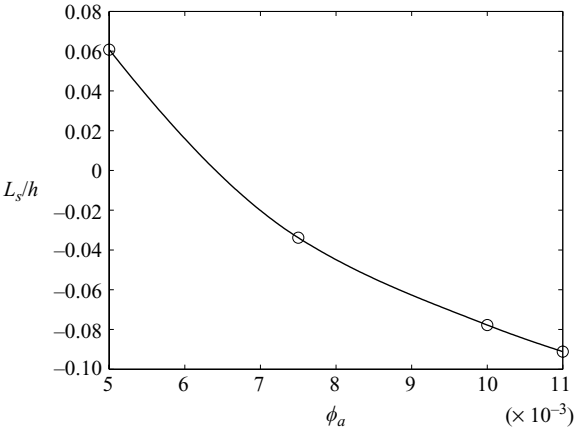

FIGURE 14. The low-shear-rate slip length versus ϕ_a for the cases depicted in figure 13.

6.4. *Effect of ϕ_a on the slip length*

To test the effect of ϕ_a, which is the non-dimensional amplitude of the potential, the following parameters are fixed: $\mu^* = 10$, $k^* = 8.5$, $m^* = n^* = 16\pi$, $b^* = 1$ and $f_w = 0.75$. Figure 13 shows the plot of slip length versus the non-dimensional shear rate at different values of ϕ_a. As expected (see Thompson & Troian 1997), the slip length increases as ϕ_a decreases. This is because the body force on the first fluid layer is smaller at smaller values of ϕ_a, thus allowing greater slip. The value of ϕ_a has no influence on the slip length at high shear rates because it depends only on f_w as discussed in the previous section. The non-dimensional shear rate at which the slip length transitions to its high-shear-rate value is approximately same for all values of ϕ_a. This implies that the effect of ϕ_{amp} on the transition is fully accounted for in the scaling of the shear rate. This further supports the estimation for the critical shear rate for transition given in (6.3).

Figure 14 shows the constant slip length at low shear rates in figure 13 as a function of ϕ_a. A nonlinear reduction in the slip length with increasing ϕ_a is observed. Further discussion on this aspect will be presented in § 6.6.

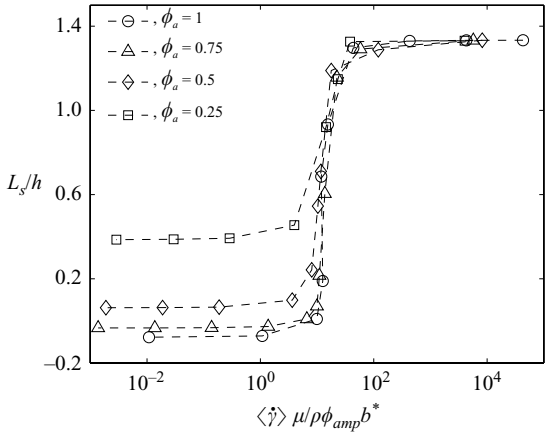

FIGURE 15. The slip length as a function of the non-dimensional shear rate for different values of b^*. The fixed parameters are $\mu^* = 10$, $\phi_a = 0.01$, $k^* = 8.5$, $m^* = n^* = 16\pi$ and $f_w = 0.75$.

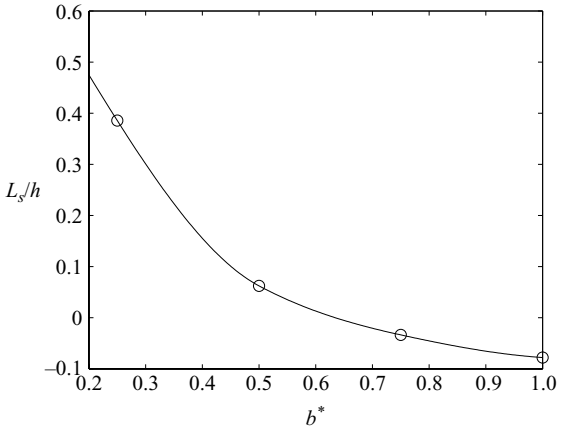

FIGURE 16. The low-shear-rate slip length versus b^* for the cases depicted in figure 15.

6.5. *Effect of b^* on the slip length*

The effect of b^* is expected to be similar to that of ϕ_a, since it also accounts for the degree of corrugation of the potential. Simulations are done with the following fixed parameters: $\mu^* = 10$, $\phi_a = 0.01$, $k^* = 8.5$, $m^* = n^* = 16\pi$ and $f_w = 0.75$. Figure 15 shows the plot of slip length versus the non-dimensional shear rate at different values of b^*.

Equation (6.3) implies that the critical shear rate for transition should scale linearly with b^*. Therefore, the shear rate plotted along the abscissa is scaled by b (note that $b = b^*$) in figure 15. Consequently, it is seen that the scaled shear rate at which the slip length transitions to its high-shear-rate value is approximately same for all values of b^*. This implies that the effect of b on the transition is fully accounted for in the scaling of the shear rate.

Figure 15 also shows that the slip length at low shear rate increases as b^* decreases. Less corrugated potential leads to greater slip at low shear rates. Figure 16 shows the constant slip length at low shear rates from figure 15 as a function of b^*. Similar to

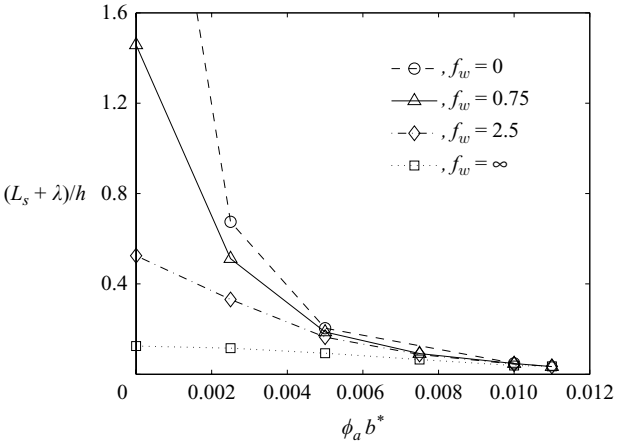

FIGURE 17. A consolidated plot of the low-shear-rate slip length versus $\phi_a b^*$ for the cases depicted in figures 13 and 15, where $f_w = 0.75$. Additional cases for different values of f_w are also shown.

the variation with ϕ_a in figure 13, a nonlinear reduction in slip length with increasing b^* is observed. The trend of low-shear-rate slip length is discussed further in the following section.

6.6. *The low-shear-rate slip length*

The variation of the low-shear-rate slip length, shown in figures 13 and 15, can be consolidated into a single figure as shown in figure 17. Additional plots for different values of f_w are also shown in the figure. It is seen that the slip length shows a nonlinear decay with respect to the amplitude $\phi_a b^*$ of the corrugation of the potential. Note that $L_s/h + \lambda/h$ has been plotted along the ordinate. As $\phi_a b^* \to 0$, the slip length $L_s/h \to 1/f_w$, as expected. This implies that if $f_w = 0$, then $L_s/h \to \infty$ when $\phi_a b^* \to 0$. For large corrugation of the potential, i.e. when $\phi_a b^* \to \infty$, the data suggest that L_s/h is close to λ/h. This corresponds to the first fluid layer becoming immobile.

This trend is consistent with the MD results by Thompson & Troian (1997) and Priezjev & Troian (2004). Specifically, we note from (6.3) that the critical shear rate for transition from the low-shear-rate to the high-shear-rate behaviour is linearly proportional to the corrugation in potential, i.e. $\langle \dot{\gamma} \rangle_{crit} \sim \phi_{amp} b$. This result together with the result in figure 17 implies that L_s/h also has a nonlinear decay of the power-law type with respect to $\langle \dot{\gamma} \rangle_{crit}$. This type of trend can be verified in the MD results of Thompson & Troian (1997) and Priezjev & Troian (2004).

An analytical solution can potentially provide a useful formula for the low-shear-rate slip length as a function of the corrugation in the potential. This is not within the scope of the present work.

7. Outlook

The *ad hoc* compressible fluid model used above captures the key features of the molecular-scale slip behaviour together with the appropriate underlying physical mechanisms. To extend the applicability of this approach, two issues need to be addressed in future work.

First, the approach above takes as input the effective potential ϕ that models the layered density field of the fluid next to wall. Additionally, it is assumed that ϕ does not change with shear rate. While this did not affect the qualitative features of the slip behaviour in comparison with the MD results, it is desirable that a fully predictive model takes as input the wall potential instead of the effective potential ϕ (see § 4 for a discussion on the difference between the effective potential and the wall potential).

Second, the fluid is governed by ideal-gas behaviour. To apply this approach to liquids a better model is recommended.

Both the above issues can be potentially addressed by using kinetic models for fluid flow at nanometre scales (see Vanderlick, Scriven & Davis 1989; Pozhar & Gubbins 1991; Guo, Zhao & Shi 2005*a* and the references therein). Specifically, Guo *et al.* (2005*a*) reported a simple kinetic model and applied it to shear flow of Lennard–Jones fluids between walls. The kinetic model is a continuum approach. The governing equations reported by Guo *et al.* (2005*a*) are similar to the equations in this work but with additional terms in the momentum equation. In the kinetic models it is not necessary to give the effective potential ϕ, like that in this work, to model the fluid layering; instead the layering effect is fundamentally resolved and obtained from the solution of the density profile for a given wall potential. The density profiles from kinetic models are reported to be in good quantitative agreement with the MD results (see Vanderlick *et al.* 1989; Guo *et al.* 2005*a*). Guo *et al.* (2005*b*) also applied this model to study the effect of temperature on liquid slip next to the walls in shear flows. They did not consider the effect of shear rate, which is the focus of our work and a key feature of the molecular-scale slip behaviour.

Thus, to make the continuum-based approach predictive, there is a way forward based on kinetic models for inhomogeneous liquids. In this work we do not use kinetic models, since they are more complex, and it was reasonable to use, as a first step, a simple continuum model to clearly identify the factors that directly contribute to the fundamental mechanisms for slip in the context of continuum equations.

The parameters that go into the kinetic models, discussed above, follow from MD parameters that are known *a priori* (see Guo *et al.* 2005*a*). Even in our simple model the input based on MD is the effective potential which can be obtained from a stationary-state MD calculation and does not require MD calculations of shear flows.

The only 'free' parameter that arises in our model is in the Navier slip boundary condition which was used to reproduce the plateau in the slip length plot at high shear rate as suggested by Lichter and co-workers (see e.g. Martini *et al.* 2008*b*). Indeed, if no such plateau is assumed, as in the MD results by Troian and co-workers (see e.g. Thompson & Troian 1997), then the parameter in the Navier slip boundary condition does not arise. Recent experiments (see e.g. Honig & Ducker 2007) suggest that appropriate values of f_w could be large corresponding to small slip lengths; however, this remain an open issue.

Current results are based on two-dimensional simulations. In case of three-dimensional simulations the slip length could be anisotropic depending on the crystal structure of the solid (Bazant & Vinogradova 2008). This case should be considered in the future.

In summary, a predictive approach based on a kinetic model that uses parameters consistent with the corresponding MD parameters should be explored in the future.

8. Conclusion

In this paper we addressed the fundamental question of whether it is possible to reproduce molecular-scale slip behaviour by using continuum equations. It was

shown that a compressible fluid model reproduces the key features of molecular-scale slip together with the underlying physical mechanisms that are consistent with those reported in prior MD studies. An incompressible fluid model is not sufficient to reproduce the mechanisms that explain slip at molecular scales. It is noted, however, that our results do not necessarily exclude the possibility that a different continuum model based on other mechanisms may reproduce the same type of molecular-scale slip behaviour.

Our model has the following features: (i) near the wall, the fluid experiences a potential; (ii) the fluid density responds to the potential; and (iii) the fluid loses momentum to the wall even at high shear rates. It was found that compressibility is important only in the near-wall region. The slip-length-versus-shear-rate trend was found to be similar to that in MD calculations. First, there is a constant value of the slip length at low shear rates. Then, the slip length increases beyond a critical shear rate. Lastly, the slip length reaches another constant value if the wall momentum loss parameter is non-zero. The scaling for the critical shear rate emerged from our results. The value of the slip length increases if the wall potential is less corrugated and if the momentum loss to the wall is low. An understanding of the overall force balance during various slip modes emerged from the governing equations. Thus, the current work helps elucidate the mechanism of slip in the context of continuum equations.

The proposed approach is potentially accessible to analytical modelling of slip at low shear rates that are relevant to technological applications.

The present work could also be useful to develop continuum simulation tools for nano-scale problems without the need for expensive hybrid computations.

We would like to acknowledge Professor S. Lichter for many insightful discussions. Support from the National Science Foundation through a CAREER grant CTS-0134546 to NAP is gratefully acknowledged.

REFERENCES

Bhushan, B. (Ed.) 2000 *Handbook of Modern Tribology*. CRC Press.

Bazant, M. Z. & Vinogradova, O. I. 2008 Tensorial hydrodynamic slip. *J. Fluid Mech.* **613**, 125–134.

Bocquet, L. & Barrat, J. L. 2007 Flow boundary conditions from nano- to micro-scales. *Soft Matt.* **3**, 685–693.

Choi, C. H., Westin, K. J. A. & Breuer, K. S. 2003 Apparent slip flow in hydrophilic and hydrophobic microchannels. *Phys. Fluids* **15**, 2897–2902.

Din, X. D. & Michaelides, E. E. 1997 Kinetic theory and molecular dynamics simulations of microscopic flows. *Phys. Fluids* **9**, 3915–3925.

Einzel, D., Panzer, P. & Liu, M. 1990 Boundary condition for fluid flow: curved or rough surfaces. *Phys. Rev. Lett.* **64**, 2269–2272.

Gao, J., Luedtke, W. D. & Landman, U. 2000 Structures, solvation forces and shear of molecular films in a rough nano-confinement. *Tribol. Lett.* **9**, 3–13.

Guo, Z., Zhao, T. S. & Shi, Y. 2005*a* Simple kinetic model for fluid flows in the nanometre scale. *Phys. Rev.* E **71**, 035301(R).

Guo, Z., Zhao, T. S. & Shi, Y. 2005*b* Temperature dependence of the velocity boundary condition for nanoscale fluid flows. *Phys. Rev.* E **72**, 036301.

Holt, J. K., Park, H. G., Wang, Y., Stadermann, M., Arthyukhin, A. B., Grigoropoulos, C. P., Noy, A. & Bakajin, O. 2006 Fast mass transport through sub-2-nanometre carbon nanotubes. *Science* **312**, 1034–1037.

Honig, C. D. F. & Ducker, W. A. 2007 No-slip hydrodynamic boundary condition for hydrophilic particles. *Phys. Rev. Lett.* **98**, 028305.

Lichter, S., Martini, A., Snurr, R. Q. & Wang, Q. 2007 Liquid slip as a rate process. *Phys. Rev. Lett.* **98**, 226001.

Lichter, S., Roxin, A. & Mandre, S. 2004 Mechanisms for liquid slip at solid surfaces. *Phys. Rev. Lett.* **93**, 086001.

Majumder, M., Chopra, N., Andrews, R. & Hinds, B. J. 2005 Nanoscale hydrodynamics: enhanced flow in carbon nanotubes. *Nature* **438**, 44–44.

Martini, A., Hsu, H. Y., Patankar, N. A. & Lichter, S. 2008*a* Slip at high shear rate. *Phys. Rev. Lett.* **100**, 206001.

Martini, A., Liu, Y., Snurr, R. Q. & Wang, Q. 2006 Molecular dynamics charaterization of thin film viscosity for EHL simulation. *Tribol. Lett.* **21**, 217–225.

Martini, A., Roxin, A., Snurr, R. Q., Wang, Q. & Lichter, S. 2008*b* Molecular mechanisms of liquid slip. *J. Fluid Mech.* **600**, 257–269.

Miksis, M. J. & Davis, S. H. 1994 Slip over rough and coated surfaces. *J. Fluid Mech.* **273**, 125–139.

Pit, R., Hervet, H. & Leger, L. 2000 Direct experimental evidence of slip in hexadecane: solid interfaces. *Phys. Rev. Lett.* **85**, 980–983.

Pozhar, L. A. & Gubbins, K. E. 1991 Dense inhomogeneous fluids: functional perturbation theory, the generalized langevin equation, and kinetic theory. *J. Chem. Phys.* **94**, 1367–1384.

Pozhar, L. A. & Gubbins, K. E. 1993 Transport theory of dense, strongly inhomogeneous fluids. *J. Chem. Phys.* **99**, 8970–8996.

Priezjev, N. V. 2007*a* Effect of surface roughness on rate-dependent slip in simple fluids. *J. Chem. Phys.* **127**, 144708.

Priezjev, N. V. 2007*b* Rate-dependent slip boundary conditions for simple fluids. *Phys. Rev.* E **75**, 051605.

Priezjev, N. V., Darhuber, A. A. & Troian, S. M. 2005 Slip behaviour in liquid films on surfaces of patterned wettability: comparison between continuum and molecular dynamics simulations. *Phys. Rev.* E **71**, 041608.

Priezjev, N. V. & Troian, S. M. 2004 Molecular origin and dynamics behaviour of slip in sheared polymer films. *Phys. Rev. Lett.* **92**, 018302.

Priezjev, N. V. & Troian, S. M. 2006 Influence of periodic wall roughness on the slip behaviour at liquid/solid interfaces: molecular-scale simulations versus continuum predictions. *J. Fluid Mech.* **554**, 25–46.

Raghunathan, A. V., Park, J. H. & Aluru, N. R. 2007 Interatomic potential-based semiclassical theory for Lennard–Jones fluids. *J. Chem. Phys.* **127**, 174701.

Sholl, D. S. & Johnson, J. K. 2006 Making high-flux membranes with carbon nanotubes. *Science* **312**, 1003–1004.

Steele, W. A. 1973 The physical interaction of gases with crystalline solids. I. gas-solid energies and properties of isolated adsorbed atoms. *Surf. Sci.* **36**, 317–352.

Thompson, P. A. & Troian, S. M. 1997 A general boundary condition for liquid flow at solid surfaces. *Nature* **389**, 360–362.

Tretheway, D. C. & Meinhart, C. D. 2002 Apparent fluid slip at hydrophobic microchannel walls. *Phys. Fluids* **14**, L9–L12.

Urbakh, M., Klafter, J., Gourdon, D. & Israelachvili, J. 2004 The nonlinear nature of friction. *Nature* **430**, 525–528.

Vanderlick, T. K., Scriven, L. E. & Davis, H. T. 1989 Molecular theories of confined fluids. *J. Chem. Phys.* **90**, 2422–2436.

Wang, C. Y. 2003 Flow over a surface with parallel grooves. *Phys. Fluids* **15**, 1114–1121.

Zhu, Y. & Granick, S. 2001 Rate-dependent slip of Newtonian liquid at smooth surfaces. *Phys. Rev. Lett.* **87**, 096105.